RSC Advances

PAPER

View Article Online
View Journal | View Issue

Cite this: *RSC Adv.*, 2025, **15**, 41139

Thermo-sensitive C_3N_4 for efficient photocatalytic degradation of methyl orange

Xuefeng Zhu,†[a] Shikai Xue,†[ab] Pingyuan Xie,[a] Qingxian Xu,[a] Yingxin Liu,[a] Chengyong Li*[a] and Qiujun Lu *[a]

The advancement of industrialization has led to severe environmental challenges stemming from inadequate pollutant management. Photocatalytic technology has emerged as a research focus due to its eco-friendly nature and high degradation efficiency. However, the widespread application of photocatalysts is hindered by limitations in recoverability and reusability. Therefore, designing high-performance photocatalysts with facile recoverability has become a critical research direction. Thermo-responsive materials, which precipitate upon heating and disperse upon cooling, offer a promising solution for enhancing recovery efficiency. In this study, a composite photocatalyst with thermo-responsive properties was successfully synthesized by combining graphite carbon nitride (g-C_3N_4) with the thermo-responsive copolymer NIPAM-DADMAC (poly(*N*-isopropylacrylamide)-*co*-diallyl dimethylammonium chloride). Key parameters including the optimal mass ratio of g-C_3N_4 to DADMAC-NIPAM, and the optimal recovery conditions were systematically determined by measuring the material's lower critical solution temperature (LCST). Experimental results demonstrated that under visible light irradiation, the composite photocatalyst achieved a remarkable 98.15% degradation rate of methyl orange (MO) within 120 min. Moreover, the composite exhibited exceptional stability and reusability, retaining over 77.92% of its degradation efficiency even after eight consecutive cycles. Additionally, its inherent thermo-responsive nature enabled highly efficient recovery of the catalyst. This research provides valuable insights and a novel strategy for the development of high-performance photocatalysts with enhanced recyclability, holding significant potential for practical applications in environmental remediation.

Received 17th July 2025
Accepted 20th October 2025

DOI: 10.1039/d5ra05141j

rsc.li/rsc-advances

1. Introduction

The increasing level of industrialization has led to a series of environmental issues resulting from the improper handling of pollutants.[1–5] Consequently, the development and application of sustainable clean energy technologies, along with their utilization in ecological remediation, have become major research focuses. Photocatalytic technology has gradually gained significant attention.[6–10] This technology utilizes solar energy to trigger the generation of photogenerated radicals, which can progressively mineralize organic pollutants in water.[11–16] This capability has promoted the development of photocatalysis as an effective pollutant removal technology. However, most reported photocatalysts suffer from low recovery rates and poor reusability.[17–20] Therefore, designing photocatalysts with excellent performance and facile recoverability has become a critical research priority.[21–23]

Since Scarpa *et al.*[24] first discovered the thermally induced phase transition behaviour of poly(*N*-isopropylacrylamide) (PNIPAM) in the 1960s, thermo-sensitive polymers of this type have consistently attracted substantial academic interest, particularly in the fields of pharmaceuticals and bioengineering.[25] As a typical thermosensitive polymer, PNIPAM exhibits unique lower critical solution temperature (LCST) behaviour.[26] Below the LCST, PNIPAM is highly soluble in water and forms a homogeneous solution; above the LCST, it undergoes a phase transition, leading to precipitation. This reversible phase transition property endows PNIPAM with excellent recyclability potential. However, the intrinsic functionality of pure PNIPAM is relatively limited, especially in terms of pollutant adsorption, which restricts its direct application in photocatalytic systems.

To further expand the functionality of PNIPAM, researchers have developed novel temperature-sensitive microgel systems through copolymerization with various hydrophilic or hydrophobic monomers.[27] Among these monomers, diallyl dimethylammonium chloride (DADMAC), a cationic monomer

[a]*College of Biological and Chemical Engineering, Changsha University, Changsha 410022, China. E-mail: lyong92@163.com; luqiujun@ccsu.edu.cn*

[b]*College of Chemistry and Bioengineering, Guilin University of Technology, Guilin 541004, China*

† Co-first authorship.

with highly hydrophilic quaternary ammonium groups, has been widely studied. When copolymerized with PNIPAM, DADMAC can form microgels that exhibit both temperature sensitivity and charge responsiveness.[28] These copolymer microgels are fully ionized in aqueous solutions, forming polymer segments with specific charge density and spacing. This charge characteristic enables them to efficiently capture charged particles or microorganisms through electrostatic interactions. Moreover, the low toxicity of these copolymers significantly enhances their advantages for applications in pharmaceutical biocompatibility and advanced drinking water treatment.

Graphite carbon nitride (g-C_3N_4) has attracted considerable attention as a promising visible-light-responsive photocatalyst due to its moderate bandgap, suitable electronic band structure, non-toxicity, and low cost.[29–33] However, like many other powdered photocatalysts, g-C_3N_4 in its pure form is prone to aggregation in aqueous solutions, and its fine powder nature makes it extremely difficult to recover from the treated water. These issues severely limit its practical application in real-world water treatment scenarios.[34–36] To address these challenges, the development of composite photocatalytic materials by integrating g-C_3N_4 with appropriate SI materials has become a current research hotspot. The goal is to combine the excellent photocatalytic performance of g-C_3N_4 with the favourable recoverability of the SI materials. Nevertheless, the application of NIPAM-*co*-DADMAC and its analogues in photocatalysis remains relatively under-explored. These copolymers have been primarily confined to adsorption applications.[37–40] The integration of these thermo-sensitive copolymers with photocatalytic matrices holds great promise in terms of photocatalytic synergy. This synergy is expected to significantly enhance the dispersion and recyclability of photocatalysts.

In this study, g-C_3N_4 was prepared by calcination. Leveraging the electrostatic interaction between g-C_3N_4 and the PNIPAM copolymer containing cationic DADMAC, a thermo-responsive g-C_3N_4/NIPAM-DADMAC composite material was synthesized, aiming to fully exploit the complementary advantages of both components. Furthermore, we investigated the mass ratio of DADMAC-NIPAM to g-C_3N_4 in the composite and the LCST of the material to determine the optimal loading ratio and recovery conditions.

2. Experimental

2.1 Preparation of g-C_3N_4

Urea (3 g) was ground and placed in an alumina crucible. The sample was heated to 520 °C at 10 °C min^{-1} and calcined for 3 h. After cooling, the sample was ground again and reheated to 500 °C at 5 °C min^{-1} for 2 h. Finally, it was naturally cooled to room temperature and ground again to obtain pale yellow g-C_3N_4 powder.

2.2 Preparation of NIPAM-*co*-DADMAC

The synthesis of NIPAM-*co*-DADMAC was based on a modified method reported by Xiang *et al.*[41] NIPAM (18.3 g) and DADMAC (17.5 mL) were dissolved in 262 mL of water in a 500 mL round-bottom flask. The solution was purged with N_2 for 30 min. Separately, potassium persulfate (KPS, 0.0351 g) and $FeCl_2 \cdot 4H_2O$ (0.0354 g) were dissolved in 4 mL and 4.75 mL of water, respectively, and then added to the flask. The mixture gradually turned yellow. The reaction was carried out at 5 °C in an ice-water bath for 2 h. The product was precipitated by adding NaCl solution, redissolved in water, and heated to 80 °C to induce reprecipitation. This purification cycle was repeated three times. The final white floccules were lyophilized to afford the thermo-responsive NIPAM-DADMAC copolymer.

2.3 Preparation of g-C_3N_4/NIPAM-DADMAC

g-C_3N_4 (15.0 mg) was dispersed in 5.0 mL of water by ultrasonication for 30 min. Separately, NIPAM-DADMAC (15.0 mg) was dissolved in 10 mL of water. The NIPAM-DADMAC solution was then added dropwise to the g-C_3N_4 dispersion, and the mixture was stirred at room temperature for 12 h to afford the g-C_3N_4/NIPAM-DADMAC composite. By varying the mass of NIPAM-DADMAC, a series of composites with mass ratios of g-C_3N_4 to NIPAM-DADMAC at 1 : 0.05, 1 : 0.1, 1 : 1, and 1 : 2 were synthesized accordingly.

2.4 Characterization

The molecular structure of NIPAM-DADMAC was characterized using nuclear magnetic resonance spectroscopy (^{1}H NMR, Varian Inova-400). Fourier transform infrared spectroscopy (FTIR, Nicolet IS10) was employed to analyse the functional groups on the material surfaces. X-ray photoelectron spectroscopy (XPS, Thermo Scientific ESCALAB Xi+) was used to determine the chemical states of elements on the catalyst surfaces. The molecular weight of the NIPAM-DADMAC material was evaluated by gel permeation chromatography (GPC, Agilent PL-GPC50). The microstructure of the catalysts was investigated by scanning electron microscopy (SEM, ZEISS Sigma 300). Zeta potential of the g-C_3N_4/NIPAM-DADMAC composites with different mass ratios was determined using a Malvern Zetasizer Nano ZS9200 (Malvern Panalytical, UK).

2.5 Photocatalytic activity evaluation

g-C_3N_4/NIPAM-DADMAC (15.0 mg) were added to 30.0 mL of a 25.0 mg L^{-1} methyl orange (MO) solution. The system was allowed to react in the dark for 90 min to establish adsorption–desorption equilibrium. Then, the photocatalytic reaction was initiated by exposing the system to visible light irradiation. A 100 W xenon lamp was used as the visible light source, and the distance between the lamp and the reaction vessel was maintained at 20 cm to ensure uniform irradiation. During the photocatalytic reaction, 2 mL samples were collected at 20 min intervals. The collected samples were immediately heated to induce precipitation of the composite photocatalyst, followed by centrifugation at 5000 rpm for 5 minutes to separate the photocatalyst from the solution. The absorbance of the resulting supernatant, which contained the residual MO, was measured using a UV-vis spectrophotometer.

3. Results and discussion

3.1 Molecular structure of NIPAM-*co*-DADMAC

The molecular structure and weight of the synthesized copolymer were characterized by nuclear magnetic resonance (NMR) spectroscopy and gel permeation chromatography (GPC). As shown in Fig. 1. The ^{1}H NMR spectrum exhibited characteristic peaks within the 1.05–7.39 ppm chemical shift range, corresponding to protons of structural units a–f in NIPAM-*co*-DADMAC (labelled in Fig. 1A), confirming successful copolymerization. GPC analysis further quantified the polymer's molecular weight distribution, revealing an average molecular weight (M_n) of 43 706 and a polydispersity index (PDI, M_w/M_n) of 2.9068, indicative of moderate chain-length uniformity.

3.2 Morphology of the photocatalysts

Scanning electron microscopy (SEM) was employed to investigate the microstructural evolution of the catalysts (Fig. 2). Pristine g-C_3N_4 exhibited smooth, micrometre-sized block-like morphologies, consistent with literature reports.[42,43] Upon incorporation of NIPAM-*co*-DADMAC, the composite surface became uniformly decorated with irregular flake-like structures, confirming the successful integration of the copolymer onto g-C_3N_4. Energy-dispersive X-ray spectroscopy (EDS) elemental mapping (Fig. 2D–F) verified the homogeneous distribution of C, N, and O throughout the composite, suggesting effective interfacial interaction between the components.

3.3 Chemical composition of the photocatalysts

X-ray photoelectron spectroscopy (XPS) and Fourier transform infrared (FTIR) spectroscopy were utilized to investigate the surface elemental composition, chemical states, and bonding configurations of the g-C_3N_4/NIPAM-*co*-DADMAC composite (Fig. 3). As shown in Fig. 3A, XPS survey spectra revealed a significant increase in nitrogen content following composite formation, attributable to the incorporation of g-C_3N_4. High-resolution C 1s and N 1s spectra (Fig. 3B and C) confirmed the coexistence of bonding signatures from both constituents: C–N bonds (286.2 eV, NIPAM-*co*-DADMAC) alongside g-C_3N_4-specific motifs (C═N–C at 288.1 eV; N–(C)$_3$ at 400.8 eV).[44–46] FTIR analysis (Fig. 3D) provided complementary evidence, with

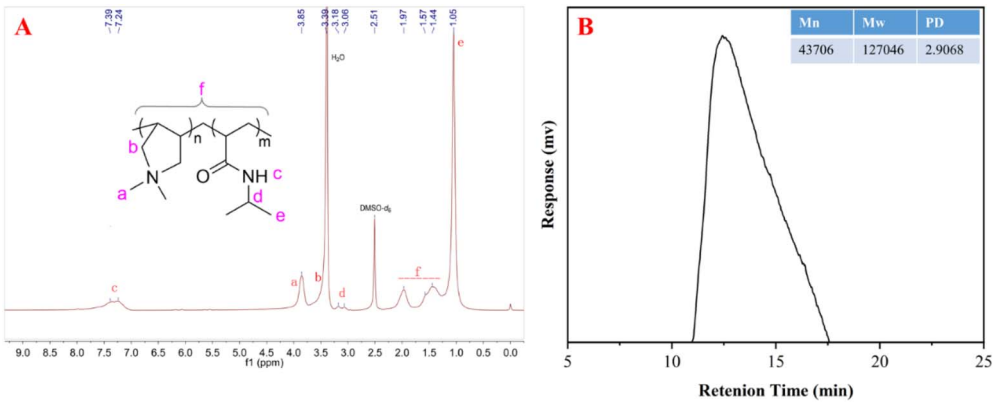

Fig. 1 (A) Nuclear magnetic resonance hydrogen spectrum and (B) gel chromatography diagram of NIPAM-DADMAC.

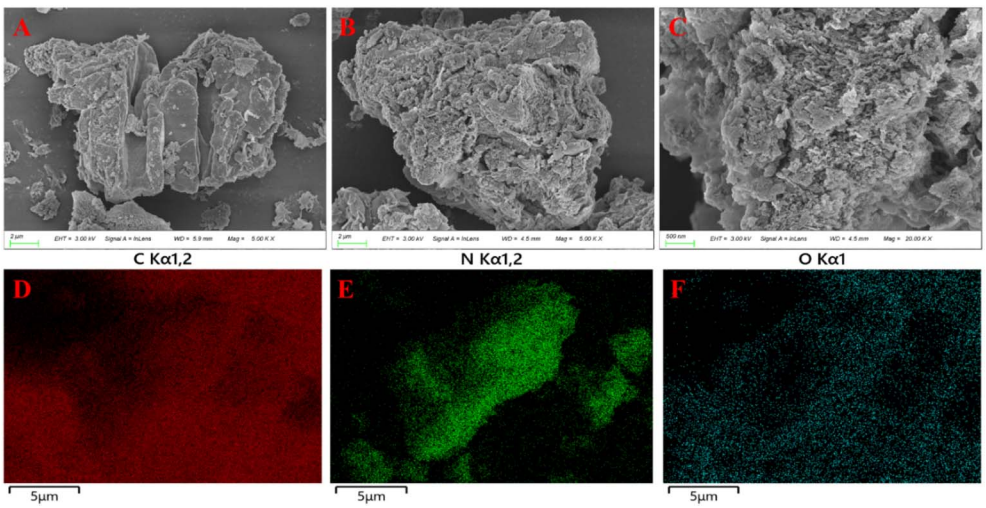

Fig. 2 (A) SEM image of g-C_3N_4, and (B and C) g-C_3N_4/NIPAM-DADMAC; (D–F) EDS image of g-C_3N_4/NIPAM-DADMAC.

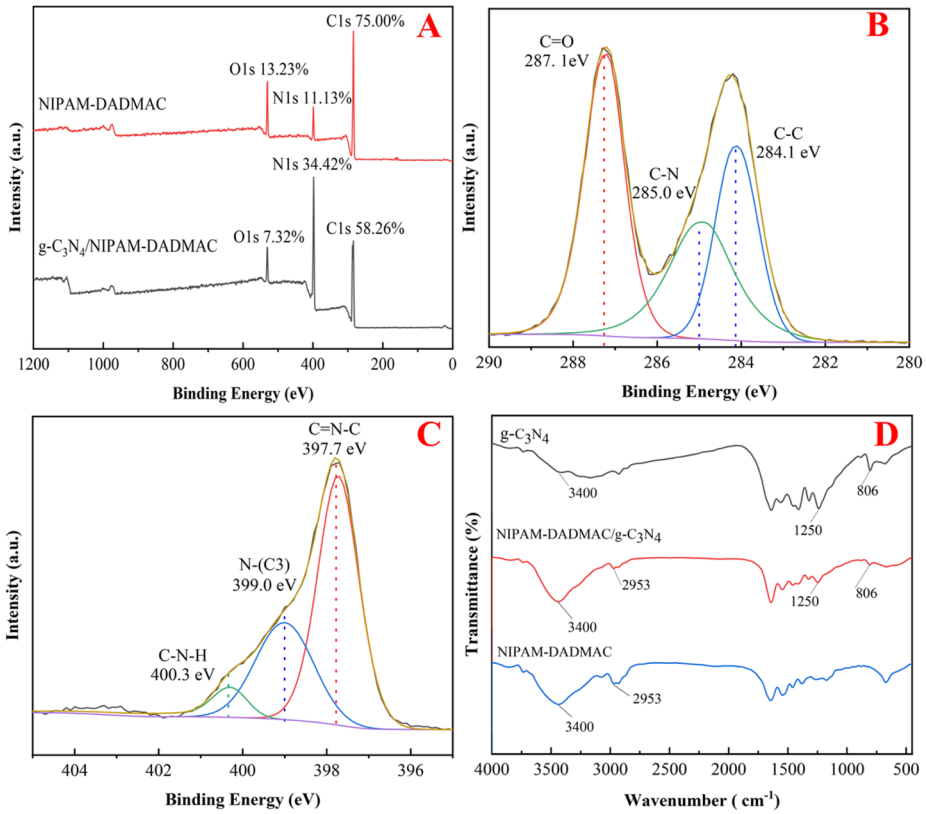

Fig. 3 (A) XPS spectra of NIPAM-DADMAC and g-C_3N_4/NIPAM-DADMAC; high-resolution (B) C 1s and (C) N 1s XPS binding energy spectra of g-C_3N_4/NIPAM-DADMAC; (D) FT-IR spectra of NIPAM-DADMAC and g-C_3N_4/NIPAM-DADMAC.

the composite spectrum exhibiting diagnostic absorption bands assignable to g-C_3N_4 (*e.g.*, 806 cm^{-1} for triazine ring modes; 1250–1650 cm^{-1} for C–N/C=N stretching) and NIPAM-*co*-DADMAC (*e.g.*, 2953 cm^{-1} for $-CH_2$; 3400 cm^{-1} for N–H bending). These collective results unambiguously validate the successful synthesis of the g-C_3N_4/NIPAM-*co*-DADMAC composite.

3.4 Zeta potential analysis

Zeta potential measurements of g-C_3N_4/NIPAM-*co*-DADMAC composites with varying mass ratios are depicted in Fig. 4. Pristine g-C_3N_4 exhibits a negative surface charge (−4.8 mV), while cationic NIPAM-*co*-DADMAC possesses inherent positive charge. To validate electrostatic-driven assembly, incremental amounts of NIPAM-*co*-DADMAC were introduced into 0.5 mg mL^{-1} g-C_3N_4 aqueous suspensions (6 mL). Systematic zeta potential analysis revealed a progressive charge reversal: increasing NIPAM-*co*-DADMAC content shifted the composite's potential from negative toward positive values (Fig. 4). At a g-C_3N_4 : NIPAM-*co*-DADMAC ratio of 0.1 : 1, the zeta potential reached a maximum of +23.2 mV. Further increases in polymer content yielded no significant potential change, indicating saturation of g-C_3N_4 surface sites. This charge reversal phenomenon confirms effective electrostatic adsorption of NIPAM-*co*-DADMAC onto g-C_3N_4, achieving successful surface modification through charge density modulation.

3.5 Dispersibility and low critical transition temperature analysis

The dispersibility of the pristine g-C_3N_4 and g-C_3N_4/NIPAM-DADMAC composite in aqueous solutions was evaluated by observing their settling behaviour after 3 days of quiescent standing. Fig. 5A shows the photographs of the two suspensions after this period. It can be clearly seen that the pristine g-C_3N_4

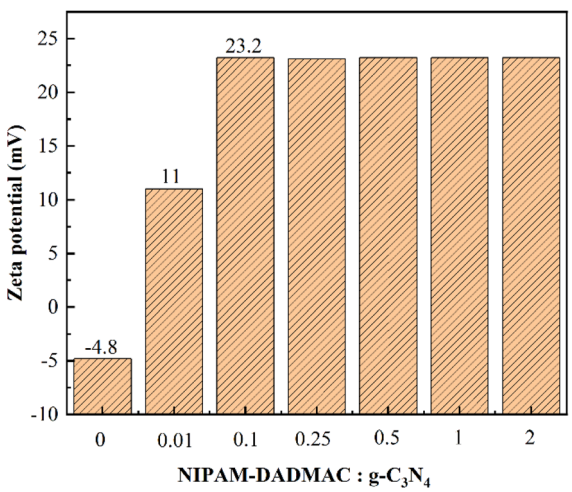

Fig. 4 Zeta potential diagrams of g-C_3N_4/NIPAM-DADMAC with different mass ratios.

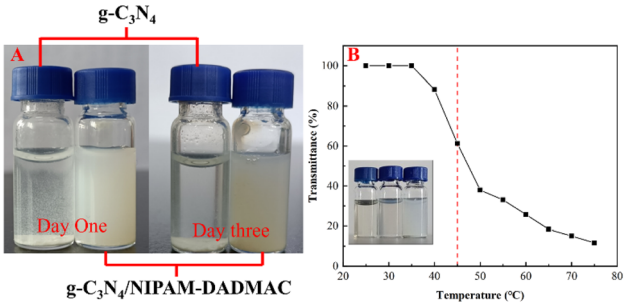

Fig. 5 (A)Comparison of the dispersibility of g-C_3N_4 and g-C_3N_4/NIPAM-DADMAC; (B) low critical transition temperature analysis diagram of NIPAM-DADMAC.

suspension exhibited significant sedimentation. A large amount of g-C_3N_4 powder settled at the bottom of the container, and a clear supernatant was formed. This poor dispersibility of pristine g-C_3N_4 is primarily due to its strong van der Waals forces and hydrogen bonding interactions between the particles, which lead to aggregation. The aggregated particles have a larger size and higher density, resulting in rapid sedimentation.

In contrast, the g-C_3N_4/NIPAM-DADMAC composite suspension maintained a homogeneous turbidity even after 3 days of standing. No obvious sedimentation was observed, indicating that the composite has excellent dispersibility in aqueous solutions. This significant improvement in dispersibility is attributed to the presence of the NIPAM-*co*-DADMAC copolymer on the surface of g-C_3N_4. The copolymer chains, which are highly soluble in water below the LCST, form a steric stabilization layer around the g-C_3N_4 particles. This layer prevents the aggregation of g-C_3N_4 particles by reducing the van der Waals forces and increasing the repulsive forces between the particles. The excellent dispersibility of the composite ensures that the photocatalytic active sites are fully exposed to the pollutant molecules and light, thereby enhancing the photocatalytic performance.

The thermo-responsive transition of NIPAM-*co*-DADMAC was quantified by temperature-dependent transmittance analysis (Fig. 5B). As the temperature increased, the transmittance of the solution began to decrease gradually. This decrease in transmittance is due to the phase transition of the copolymer. Above the LCST, the copolymer chains undergo a conformational change, transitioning from an extended, hydrophilic state to a collapsed, hydrophobic state. The hydrophobic copolymer chains then aggregate together, forming large particles that scatter light, resulting in a decrease in transmittance. The inflection point in the transmittance–temperature curve, which corresponds to the temperature at which the transmittance decreases by 50%, is defined as the LCST of the copolymer. From Fig. 5B, it can be determined that the LCST of the NIPAM-DADMAC copolymer is approximately 45 °C.

3.6 Ultraviolet diffuse reflectance and photoluminescence analysis

The optical properties of photocatalysts, including their light absorption capacity and charge separation efficiency, are crucial factors that directly influence their photocatalytic performance. In this study, ultraviolet diffuse reflectance spectroscopy (UV-DRS) and photoluminescence (PL) spectroscopy were employed to investigate the optical properties of the pristine g-C_3N_4 and g-C_3N_4/NIPAM-DADMAC composite.

Fig. S1A shows the UV-DRS spectra of the pristine g-C_3N_4 and g-C_3N_4/NIPAM-DADMAC composite. It can be observed that the UV-DRS spectrum of the composite closely resembles that of the pristine g-C_3N_4. Fig. S1B shows that the bandgap energy of the composite is virtually identical to that of the pristine g-C_3N_4. This indicates that the hybridization of g-C_3N_4 with the NIPAM-*co*-DADMAC copolymer does not appreciably perturb the electronic structure of the g-C_3N_4 framework. In addition, the photoluminescence (PL) spectra of g-C_3N_4 and g-C_3N_4/NIPAM-DADMAC composites were also determined. As shown in Fig. S1C, there was no significant intensity difference in the PL spectra of g-C_3N_4 and g-C_3N_4/NIPAM-DADMAC composites, further indicating that the hybridization of g-C_3N_4 with NIPAM-*co*-DADMAC copolymer had no obvious effect on the electronic structure of the g-C_3N_4 framework and still maintained a similar charge separation efficiency. Overall, the results of UV-DRS and PL analysis indicated that the combination of NIPAM-DADMAC copolymer with g-C_3N_4 did not weaken the light absorption ability of g-C_3N_4. These optical properties laid a good foundation for the excellent photocatalytic performance of the composites.

3.7 Photocatalytic activity assessment

The photocatalytic activity of the g-C_3N_4/NIPAM-DADMAC composite was systematically evaluated by measuring the degradation rate of methyl orange (MO) under visible light irradiation. A series of experiments were conducted to investigate the effects of different parameters, including the mass ratio of g-C_3N_4 to NIPAM-DADMAC and the reaction temperature on the photocatalytic performance of the composite. Prior to photocatalytic testing, the reaction system underwent a 90 min dark adsorption period to establish adsorption–desorption equilibrium.

Fig. 6A compares the MO degradation performance of g-C_3N_4/NIPAM-DADMAC composites at varying mass ratios under visible light irradiation. It can be clearly observed that the mass ratio has a significant impact on the photocatalytic activity of the composite. After 20 min of visible light irradiation, the composite with a mass ratio of 1 : 0.1 (g-C_3N_4 : NIPAM-DADMAC) exhibited the fastest degradation rate of MO, with a degradation rate of approximately 54.01%. In contrast, the composites with other mass ratios (1 : 0.05, 1 : 1, and 1 : 2) demonstrated relatively slower degradation rates, with degradation rates of around 39.66%, 42.10%, and 46.43%, respectively. With the extension of the irradiation time to 120 min, the composite with the 1 : 0.1 mass ratio achieved the highest degradation efficiency of 98.15%. The composites with the 1 : 0.05, 1 : 1, and 1 : 2 mass ratios reached degradation efficiencies of 97.45%, 96.28%, and 89.58%, respectively. These results clearly indicate that the composite with the 1 : 0.1 mass ratio has the best photocatalytic activity among all the tested samples.

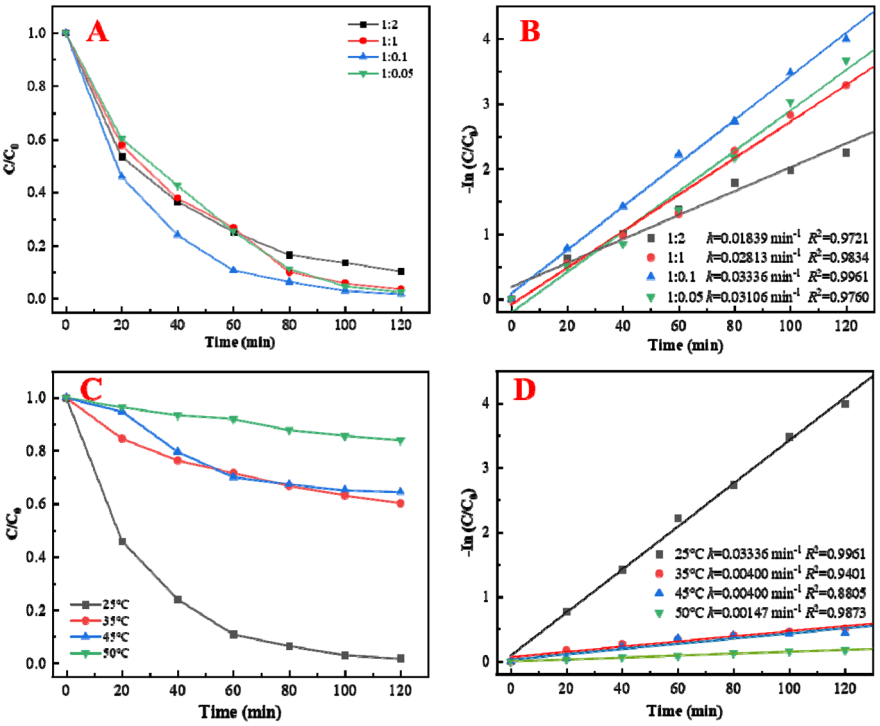

Fig. 6 (A) Methyl orange degradation rate curve, and (B) corresponding photodegradation kinetic curve for g-C_3N_4/NIPAM-DADMAC at different catalyst loadings; (C) methyl orange degradation rate curve, and (D) corresponding photodegradation kinetic curve for g-C_3N_4/NIPAM-DADMAC at different degradation temperatures.

To further analyze the photocatalytic kinetics, the degradation data were fitted using the pseudo-first-order kinetic model, which is commonly used to describe the photocatalytic degradation of organic pollutants.[47–50] The pseudo-first-order kinetic equation is expressed as:

$$-\mathrm{Ln}(C/C_0) = kt$$

where k is the pseudo-first-order rate constant (min^{-1}), t is the reaction time (min), C_0 is the initial concentration of MO after adsorption equilibrium, and C is the concentration of MO at time t.

Fig. 6B shows the corresponding pseudo-first-order kinetic curves for the composites with different mass ratios. The composite with the 1 : 0.1 mass ratio has the highest rate constant of 0.03336 min^{-1}, which is significantly higher than those of the other composites (0.03106 min^{-1} for 1 : 0.05, 0.02813 min^{-1} for 1 : 1, and 0.01839 min^{-1} for 1 : 2). This further confirms that the 1 : 0.1 mass ratio is the optimal ratio for the composite to exhibit the best photocatalytic performance.

The reason for the optimal mass ratio can be explained as follows: when the amount of NIPAM-DADMAC copolymer is too low (mass ratio 1 : 0.05), the copolymer cannot fully cover the surface of g-C_3N_4. As a result, the dispersibility of the composite is poor, and the adsorption capacity for MO is limited, leading to lower photocatalytic activity. When the amount of copolymer is too high (mass ratios 1 : 1 and 1 : 2), the excess copolymer may cover the active sites of g-C_3N_4, blocking the light absorption and reducing the number of available photogenerated electron–hole pairs. Additionally, the excess copolymer may form a thick layer on the surface of g-C_3N_4, increasing the charge transfer resistance and promoting the recombination of photogenerated charges. Therefore, the composite with the 1 : 0.1 mass ratio has the optimal balance between the dispersibility, adsorption capacity, and active site exposure, resulting in the highest photocatalytic activity.

The reaction temperature is another important parameter that can affect the photocatalytic activity of the composite. Fig. 6C shows the degradation rate curves of MO at different temperatures. It can be observed that the reaction temperature has a significant impact on the degradation efficiency, and the degradation efficiency decreases as the temperature rises. The corresponding pseudo-first-order kinetic curves are shown in Fig. 6D. The rate constants gradually decrease with the increase of temperature, being 0.00400 min^{-1} at 35 °C, 0.00400 min^{-1} at 45 °C, and 0.00147 min^{-1} at 50 °C, respectively.

The decrease in photocatalytic activity at higher temperatures can be attributed to the phase transition and precipitation of the NIPAM-*co*-DADMAC copolymer above the LCST (45 °C). This precipitation leads to the aggregation of the composite material, thereby reducing the specific surface area and the exposure of active sites.

To further confirm that the degradation efficiency decreases with the increase in temperature, additional experiments on the degradation of rhodamine B (another common dye pollutant) at different temperatures were conducted. The results (Fig. S2) showed a similar trend.

Table 1 Removal rate of different photocatalytic materials for ye-type pollutants removal

Sample	Catalyst dosage (g L^{-1})	Pollutant	Pollutant concentration (mg L^{-1})	Light source	Photocatalytic degradation time (min)	Removal rate	Recyclability	Ref.
Co/P–C_3N_4	1.00	Methyl orange	10	300 W mercury lamp	120	70%	—	51
C_3N_4/$AlFeO_3$	1.00	Methyl orange	20	500 W xenon lamp	60	97%	91% (5th)	52
Bi@BiOCl/C_3N_4-DPY	0.67	Methyl orange	10	500 W xenon lamp	180	84.5%	82% (4th)	53
BiO–Ag(0)/C_3N_4@ZIF-67	1.0	Congo red	40	Solar	150	90.0%	78.2% (4th)	54
g-C_3N_4/NIPAM-DADMAC	0.5	Methyl orange	25	100 W deuterium lamp	120	98%	77.92% (8th)	This work

To evaluate the performance of the g-C_3N_4/NIPAM-DADMAC composite in comparison with other reported photocatalytic materials, a comprehensive comparison was conducted based on key parameters such as photocatalyst dosage, pollutant concentration, degradation time, removal rate, and recyclability. The results are summarized in Table 1.

3.8 Reusability evaluation of the catalyst

The reusability of a photocatalyst is a key factor in determining its practical application potential. A photocatalyst with good reusability can significantly reduce the treatment cost. In this study, the reusability of the thermo-sensitive g-C_3N_4/NIPAM-DADMAC composite (with the optimal 1 : 0.1 mass ratio) was evaluated by repeating the photocatalytic degradation experiment of MO for multiple cycles.

Fig. 7 shows the schematic diagram of the cyclic photocatalytic process and the degradation efficiency of the composite over 8 consecutive cycles. After each photocatalytic cycle, the composite was recovered through a simple thermo-responsive precipitation process: the temperature of the reaction solution was raised to LCST of the copolymer, causing the composite to precipitate. The precipitated composite was then separated from the solution by centrifugation at 5000 rpm for 5 min, washed thoroughly with deionized water three times to remove any residual MO molecules and by-products, and then reused in the next cycle under the same experimental conditions. As shown in Fig. 7, the composite exhibited excellent reusability, even after eight successive cycles, the photocatalytic efficiency of the composite was still as high as 77.92%.

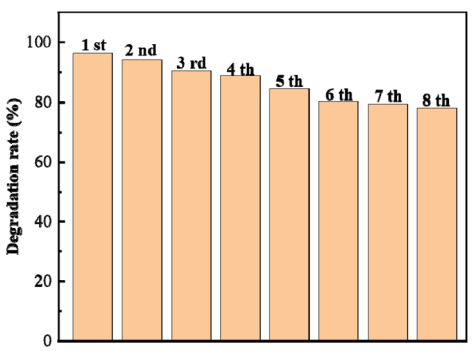

Fig. 7 The cyclic photocatalytic degradation efficiency of MO by g-C_3N_4/NIPAM-DADMAC.

This gradual decline in degradation efficiency is a common phenomenon in cyclic photocatalytic experiments and can be attributed to cumulative occupation of active sites, partial catalyst leaching, and structural changes. To exclude structural alteration as the primary cause of the activity loss, the FTIR spectra of the fresh and used composite (after 8 cycles) were compared. Fig. S3 shows the FTIR spectra of the two samples. It can be observed that there are no discernible changes in the characteristic absorption bands of the composite. The peaks corresponding to g-C_3N_4 (806 cm^{-1} for triazine ring bending, 1250–1650 cm^{-1} for C–N/C=N stretching) and the NIPAM-DADMAC copolymer (2953 cm^{-1} for C–H stretching, 3400 cm^{-1} for N–H stretching) are still present and have the same intensity and position in both spectra. This indicates that the framework structure of the composite remains intact throughout the 8 cycles of photocatalytic reaction and recovery. Therefore, the main cause of the loss of activity might be the cumulative occupation of active sites by pollutants and the loss of some catalysts, rather than structural decomposition.

The excellent reusability of the g-C_3N_4/NIPAM-DADMAC composite, combined with the simple and energy-efficient thermal recovery protocol, makes it a highly promising candidate for practical and sustainable water treatment applications. The ability to reuse the composite for multiple cycles not only reduces the cost of the photocatalytic process but also minimizes the environmental impact associated with the disposal of used photocatalysts.

3.9 Universal experiment on photocatalytic degradation

To assess the broader applicability of the g-C_3N_4/NIPAM-DADMAC composite, its photocatalytic activity was tested against a variety of representative pollutants, including cationic dyes (rhodamine B), anionic azo dyes (Congo red), and antibiotic pollutants (tetracycline hydrochloride).

As shown in Fig. S4, within 120 min of illumination, the removal efficiency of this composite material for rhodamine B was approximately 94.2%, for tetracycline hydrochloride was 70.1%, and for Congo red was 45.2%, highlighting its wide applicability to various water pollutants. These results clearly demonstrate the versatility of the g-C_3N_4/NIPAM-DADMAC composite in degrading diverse aquatic pollutants. This broad applicability significantly enhances the practical value of the composite in environmental remediation.

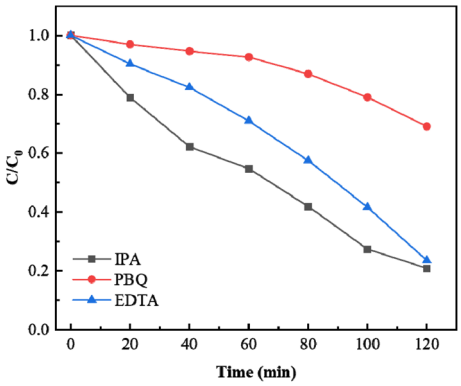

Fig. 8 Free radical trapping experiment of g-C_3N_4/NIPAM-DADMAC for the degradation of MO.

3.10 Mechanism research

Active species trapping experiments were conducted to identify the primary active radicals involved in the photocatalytic degradation of methyl orange by the g-C_3N_4/NIPAM-DADMAC composite.

Three common trapping agents were used in the experiments: isopropanol (IPA) was used to trap hydroxyl radicals ($^{\bullet}OH$), *para*-benzoquinone (PBQ) was used to trap superoxide radicals ($^{\bullet}O_2^-$), and ethylenediaminetetraacetic acid disodium salt (EDTA) was used to trap photogenerated holes (h^+). The trapping experiments were carried out under the same optimal conditions as the photocatalytic activity evaluation.

Fig. 8 shows the results of the trapping experiments. When IPA was added to trap $^{\bullet}OH$, the degradation rate of MO slightly decreased to approximately 79.20%. This indicates that $^{\bullet}OH$ plays a minor role in the photocatalytic degradation process. When EDTA was added to trap h^+, the degradation rate further decreased to around 76.53%, suggesting that h^+ contributes more to the degradation than $^{\bullet}OH$.

In contrast, when PBQ was added to trap $^{\bullet}O_2^-$, the degradation rate of MO was almost completely inhibited, with a degradation rate of only about 30.93%. This significant inhibition clearly indicates that $^{\bullet}O_2^-$ is the primary active radical responsible for the photocatalytic degradation of MO by the composite.

4. Conclusions

In summary, a thermo-responsive g-C_3N_4/NIPAM-DADMAC composite photocatalyst was successfully synthesized through a simple and efficient method. The composite exhibited excellent dispersibility in aqueous solutions below the LCST of the copolymer and could be efficiently recovered by heating above the LCST (45 °C). The photocatalytic activity was evaluated through MO degradation under visible light. The optimal composite, with a g-C_3N_4 to NIPAM-DADMAC mass ratio of 1 : 0.1, achieved 98.15% degradation in 120 min at 25 °C. It exhibited excellent stability and retained 77.92% efficiency after eight cycles. The composite demonstrated broad applicability in degrading various pollutants, including rhodamine B, tetracycline hydrochloride, and Congo red. Active species trapping experiments indicated that $^{\bullet}O_2^-$ were the primary active radicals responsible for the photocatalytic degradation process. This work establishes that strategic integration of thermo-sensitive polymers with semiconductor photocatalysts effectively reconciles the traditional trade-off between high catalytic activity and practical recoverability. The demonstrated synergy of electrostatic assembly and LCST-mediated recovery presents a viable design strategy for next-generation smart photocatalytic systems in sustainable water remediation.

Author contributions

Xuefeng Zhu: data curation, formal analysis, investigation, validation, resources, writing – original draft; Shikai Xue: data curation, formal analysis, investigation, validation, writing – original draft; Pingyuan Xie: data curation, formal analysis, resources; Qingxian Xu: data curation, formal analysis; Yingxin Liu: resources, supervision, methodology; Chengyong Li: resources, supervision, methodology, writing – review & editing; Qiujun Lu: resources, funding acquisition, supervision, methodology, writing – review & editing.

Conflicts of interest

There are no conflicts to declare.

Data availability

Additional datasets generated and analysed during the current study are available from the corresponding author upon reasonable request.

Supplementary information is available. See DOI: **https://doi.org/10.1039/d5ra05141j**.

Acknowledgements

This work was supported by the National Natural Science Foundation of China (32303040), the Changsha Science and Technology Plan Project (kq2506024), the Innovation Training Program for College Students in Hunan Province (5003).

Notes and references

1 P. Wang, C. Xu, X. Zhang, Q. Yuan and S. Shan, *Environ. Res.*, 2023, **223**, 115467.
2 P. Su, C. Zhang, Y. Liu, J. Zhang, R. Djellabi, R. Wang, J. Guo, R. Zhang, H. Guo, X. Ding and X. Liu, *J. Environ. Chem. Eng.*, 2023, **11**, 110765.
3 X. Hu, G. Wang, J. Wang, Z. Hu and Y. Su, *Appl. Surf. Sci.*, 2020, **511**, 145499.
4 N. Siddique, M. I. Din, R. Khalid and Z. Hussain, *Rev. Chem. Eng.*, 2024, **40**, 481–510.
5 V. Tiwari, B. Pal and S. Kaur, *Sol. Energy*, 2025, **296**, 113587.
6 Y. Li, M. Gu, T. Shi, W. Cui, X. Zhang, F. Dong, J. Cheng, J. Fan and K. Lv, *Appl. Catal., B*, 2020, **262**, 118281.

7 Y. Luo, R. Peng, Q. Cui, P. Niu and L. Li, *ACS Appl. Mater. Interfaces*, 2021, **13**, 60471–60477.
8 X. Wang, S. Li, P. Chen, F. Li, X. Hu and T. Hua, *Mater. Today Chem.*, 2022, **23**, 100650.
9 H. Fei, J. Wu, J. Zhang, T. Zhao, W. Guo, X. Wang, S. Yang and G. Liu, *J. Build. Eng.*, 2024, **97**, 110782.
10 S. Kalikeri and V. S. Kodialbail, *Surf. Interfaces*, 2023, **36**, 102492.
11 D. Zhu, S. Xue, S. Yang, Q. Zuo, H. Wang, Q. Lu, G. Ruan, C. Zhao and F. Du, *Chem. Eng. J.*, 2023, **476**, 146681.
12 Y. Wang, C. Liu, H. Hu, Q. Lu, H. Wang, C. Zhao, F. Du and N. Tang, *J. Environ. Sci.*, 2024, **136**, 547–558.
13 T. Hussain, M. Hussain, S. Hussain and M. Kaseem, *Sep. Purif. Technol.*, 2022, **282**, 120025.
14 D. Liu, L. Jiang, D. Chen, Z. Hao, B. Deng, Y. Sun, X. Liu, B. Jia, L. Chen and H. Liu, *Chem. Eng. J.*, 2024, **482**, 149165.
15 J. Qiu, M. Li, J. Xu, X.-F. Zhang and J. Yao, *J. Hazard. Mater.*, 2020, **389**, 121858.
16 L. Zhang, F. Song, J. Yu, R. Chen, G. Sun, Q. Liu, J. Liu, H. Zhang and J. Wang, *Appl. Surf. Sci.*, 2021, **563**, 150305.
17 J. Zhang, H. Wu, L. Shi, Z. Wu, S. Zhang, S. Wang and H. Sun, *Sep. Purif. Technol.*, 2024, **329**, 125225.
18 M. Golshan, B. Kakavandi, M. Ahmadi and M. Azizi, *J. Hazard. Mater.*, 2018, **359**, 325–337.
19 D. Zhu, S. Xue, S. Yang, Q. Zuo, H. Wang, Q. Lu, G. Ruan, C. Zhao and F. Du, *Chem. Eng. J.*, 2023, **476**, 146681.
20 R. Zhao, X. Shi, T. Ma, H. Rong, Z. Wang, F. Cui, G. Zhu and C. Wang, *ACS Appl. Mater. Interfaces*, 2021, **13**, 755–764.
21 D. D. La, C. V. Tran, N. T. T. Hoang, M. D. Doan Ngoc, T. H. P. Nguyen, H. T. Vo, P. H. Ho, T. A. Nguyen, S. V. Bhosale, X. C. Nguyen, S. W. Chang, W. J. Chung and D. D. Nguyen, *Fuel*, 2020, **281**, 118655.
22 S. Xue, X. Li, L. Li, S. Huang, J. Luo, H. Wang, Q. Lu, G. Yin and F. Du, *Appl. Surf. Sci.*, 2025, **704**, 163431.
23 S. Xue, D. Zhu, Q. Zuo, S. Yang, H. Wang, Q. Lu, G. Yin, G. Ruan and F. Du, *New J. Chem.*, 2024, **48**, 9185–9195.
24 J. S. Scarpa, D. D. Mueller and I. M. Klotz, *J. Am. Chem. Soc.*, 1967, **89**, 6024–6030.
25 F. Rahmani, R. Atabaki, S. Behrouzi, F. Mohamadpour and H. Kamali, *Int. J. Pharm.*, 2023, **631**, 122484.
26 Y. Yu, Y. Cheng, J. Tong, L. Zhang, Y. Wei and M. Tian, *J. Mater. Chem. B*, 2021, **9**, 2979–2992.
27 Y. Pan, H. Bao, N. G. Sahoo, T. Wu and L. Li, *Adv. Funct. Mater.*, 2011, **21**, 2754–2763.
28 X. Wang, W. Gao, B. Liao and P. Fatehi, *ACS Omega*, 2023, **8**, 27156–27169.
29 X. Qian, W. Li, X. Wang, H. Guan, Q. Bao, B. Zhao, B. Wulan, S. Liu, D. Zhu, X. Feng and J. Sun, *Adv. Funct. Mater.*, 2025, **35**, 2416946.
30 P. Su, J. Zhang, K. Xiao, S. Zhao, R. Djellabi, X. Li, B. Yang and X. Zhao, *Chin. J. Catal.*, 2020, **41**, 1894–1905.
31 J. Singh, S. Akhtar, T. T. Tran and J. Kim, *J. Alloys Compd.*, 2023, **954**, 170206.
32 Y. Nie, R. Bao, X. Xiao, J. Yi and G. Xu, *Surf. Interfaces*, 2024, **55**, 105343.
33 X. Xu, Y. Xiao, X. Xu, S. A. C. Carabineiro and J. Zhu, *J Materiomics*, 2025, **11**, 100969.
34 Y. Yao, F. Lu, Y. Zhu, F. Wei, X. Liu, C. Lian and S. Wang, *J. Hazard. Mater.*, 2015, **297**, 224–233.
35 Y. Dong, X. Wang, H. Sun, X. Zhao, H. Zhang, L. Chen, D. Huang, Y. Yang, J. Zheng and L. Wang, *J. Membr. Sci.*, 2024, **709**, 123154.
36 P. Lin, X. Lu, B. J. Deka, J. Shang, H. Wu, J. Sun, C. Yi, M. U. Farid, A. K. An and J. Guo, *Sep. Purif. Technol.*, 2025, **356**, 129948.
37 J. Lin, Y. Guo, M. Chen, Y. Liu, S. Xiang, P. Wang, Z. Fei, X. Miao and S. Hua, *J. Ind. Eng. Chem.*, 2024, **138**, 502–515.
38 D. Zheng, K. Wang, B. Bai, N. Hu and H. Wang, *Carbohydr. Polym.*, 2022, **282**, 119113.
39 H. Bai, Q. Zhang, T. He, G. Zheng, G. Zhang, L. Zheng and S. Ma, *Appl. Clay Sci.*, 2016, **124–125**, 157–166.
40 A. M. Atta, S. A. Al-Hussain, H. A. Al-Lohedan, A. O. Ezzat, A. M. Tawfeek and T. Al-Otabi, *Polym. Int.*, 2018, **67**, 471–480.
41 Y. Xiang, M. K. Banks, R. Wu, W. Xu and S. Chen, *Mater. Chem. Phys.*, 2018, **220**, 58–65.
42 Y. Bu, Z. Chen, T. Xie, W. Li and J.-P. Ao, *RSC Adv.*, 2016, **6**, 47813–47819.
43 S. Qing, H. Chen, L.-j. Han, Z. Ye, L. Shi, Z. Shu, L. Chen, L. Xu and Q. Xu, *ACS Omega*, 2020, **5**, 27873–27879.
44 Q. Li, P. Shen, Y. Tian, X. Li and K. Chu, *J. Colloid Interface Sci.*, 2022, **606**, 204–212.
45 Y.-J. Yuan, Z. Shen, S. Wu, Y. Su, L. Pei, Z. Ji, M. Ding, W. Bai, Y. Chen, Z.-T. Yu and Z. Zou, *Appl. Catal., B*, 2019, **246**, 120–128.
46 B. Zhang, R. Wang, B. Liu, X. Wang, Y. Guo and L. Zhang, *J. Alloys Compd.*, 2025, **1020**, 179462.
47 F. Zhang, Y. Sun, D. Zhang, Z. Chen, F. Liu, Y. Yuan and S. Liu, *Colloids Surf., A*, 2025, **705**, 135761.
48 Z. Yang, J. Yuan, C. Zhong, X. Hou, Q. Sun, M. Zhang, Y. Wu, X. Wang, S. Guo and T. Long, *ChemistrySelect*, 2025, **10**, e202406032.
49 A. Mallah, E. A. Abdelrahman, N. Raza, L. S. Alqarni, M. Ismail, A. Modwi, E. S. Al-Farraj, M. G. Ghoniem and M. Khairy, *Inorg. Chem. Commun.*, 2024, **170**, 113464.
50 N. Pourshirband, A. Nezamzadeh-Ejhieh and S. N. Mirsattari, *Spectrochim. Acta, Part A*, 2021, **248**, 119110.
51 X. Yu, L. Gao, Q. Wang, Z. Chi and H. Li, *Colloids Surf., A*, 2025, **717**, 136818.
52 L. Jianmin, Y. He and Y. Zhao, *Russ. J. Phys. Chem. A*, 2024, **98**, 2380–2389.
53 W. Yang, Y. Gao and M. Cao, *Langmuir*, 2023, **39**, 18342–18353.
54 O. P. Kumar, M. Ahmad, M. A. Nazir, A. Anum, M. Jamshaid, S. S. A. Shah and A. Rehman, *Environ. Sci. Pollut. Res.*, 2022, **29**, 35300–35313.